

Hierarchical bayesian inference: constraining population distribution of dark matter halo shapes via stellar streams

David Chemaly¹*, Elisabeth Sola¹, Vasily Belokurov¹, Sergey E. Koposov^{1,2}, GyuChul Meyong¹,

HanYuan Zhang¹, Denis Erkal³

¹ Institute of Astronomy, Madingley Rd, Cambridge CB3 0HA, UK

² Institute for Astronomy, University of Edinburgh, Royal Observatory, Blackford Hill, Edinburgh EH9 3HJ, UK

³ Department of Physics, University of Surrey, Guildford, GU2 7XH, Surrey, UK

arXiv:2601.15373v1 [astro-ph.GA] 21 Jan 2026

Accepted XXX. Received YYY; in original form ZZZ

ABSTRACT

Stellar streams, the debris of tidally disrupted satellites, trace their host’s gravitational potential and thus probe dark matter halo structure. While six-dimensional phase-space data of Galactic streams enable precise dark matter halo modelling in the Milky Way, streams around external galaxies are typically available only as low surface brightness features without kinematics (i.e. two-dimensional photometric data), providing only weak constraints when considered individually. We present a hierarchical Bayesian framework that infers the population distribution of halo flattening using only projected stream tracks. Streams are forward-modelled in **StreaMAX** , a new JAX-accelerated particle-spray package that achieves orders of magnitude faster stream generation when compared to traditional methods. For each stream we fit an axisymmetric dark matter halo model and obtain a posterior on the flattening. These posteriors are then combined through hierarchical reweighting to constrain the population distribution. Using mock data, we show that individual fits recover the correct flattening with modest precision and exhibit projection-induced multi-modalities. Nevertheless, aggregating these fits yields accurate and confident constraints on the underlying population distribution of dark matter halo morphologies, clearly distinguishing between oblate, spherical, and prolate populations. The total computational cost scales linearly with sample size. Our results demonstrate that ensembles of purely photometric streams carry sufficient information to constrain dark matter halo shapes in external galaxies at the population level. With the forthcoming samples from Euclid and Rubin/LSST, this approach offers a practical path to population-level inferences of halo morphology without any kinematic measurements.

Key words: galaxies: haloes – galaxies: interactions – galaxies: statistics – cosmology: dark matter

1 INTRODUCTION

Stellar streams, elongated structures formed when dwarf galaxies or globular clusters are tidally disrupted by their host’s gravitational field, are powerful probes of galactic potentials and tracers of galaxy assembly (Johnston et al. 1995; Helmi & White 1999). As satellites orbit their hosts, tidal forces strip stars from the progenitor galaxy, producing coherent, narrow features that approximately follow the progenitor’s orbit and can persist for gigayears, retaining dynamical memory of their past trajectories (Johnston et al. 1995; Helmi & White 1999; Bullock & Johnston 2005). Because these trajectories depend sensitively on the underlying gravitational potential, streams provide robust constraints on mass distributions, especially dark matter (DM) haloes informing parameters such as halo mass, concentration, and shape (e.g., Ibata et al. 2001; Law & Majewski 2010; Koposov et al. 2010; Belokurov et al. 2014; Gibbons et al. 2014; Bonaca & Hogg 2018). Streams also serve as fossil records of accretion, enabling reconstructions of merger histories and halo

growth (e.g., Bullock & Johnston 2005; Deason & Belokurov 2024; Bonaca & Price-Whelan 2025).

Early theoretical work and simulations established the sensitivity of streams to host mass distributions over large radial ranges (Johnston et al. 1995; Helmi & White 1999; Johnston et al. 2001; Ibata et al. 2001). Subsequent surveys and follow-up observations (e.g., Grillmair & Dionatos 2006; Malhan et al. 2018; Shipp et al. 2018; Li et al. 2022) have leverage stream morphology and kinematics to probe the potential of the Milky Way (MW) in detail (e.g., Koposov et al. 2010; Price-Whelan et al. 2014; Price-Whelan & Bonaca 2018). Dynamically cold, thin streams from globular clusters respond to subtle variations in the local gravitational field, exhibiting gaps, spurs, and track curvature changes that encode small scale perturbations such as dark matter subhaloes (e.g., Ibata et al. 2002; Johnston et al. 2002; Yoon et al. 2011; Carlberg et al. 2012; Erkal & Belokurov 2015; Bovy et al. 2016; Erkal et al. 2017; Banik & Bovy 2019). By contrast, broader, dynamically hotter streams from dwarf galaxy progenitors constrain halo shape and mass on larger spatial scales (e.g. Johnston et al. 2005; Law & Majewski 2010; Pearson et al. 2015; Gibbons et al. 2014; Erkal et al. 2019; Vasiliev et al. 2021).

* E-mail: dc824@cam.ac.uk

Within Λ CDM, halos are approximately self-similar across mass scales: they follow universal density profiles (Navarro et al. 1997; Zhao et al. 2003; Ludlow et al. 2014), follow a mass–concentration relation (Wechsler et al. 2002; Macciò et al. 2008; Dutton & Macciò 2014; Diemer & Kravtsov 2015), and are intrinsically triaxial if baryons are neglected (Jing & Suto 2002a; Allgood et al. 2006; Despali et al. 2014; Bonamigo et al. 2015). Real galaxies, however, deviate from this idealised picture. Baryonic physics (adiabatic contraction, feedback-driven core formation) can reshape inner density profiles and axis ratios (Blumenthal et al. 1986; Gnedin et al. 2004; Bryan et al. 2013; Di Cintio et al. 2014; Chua et al. 2019; Prada et al. 2019); merger histories modulate triaxiality and concentration scatter (Boylan-Kolchin et al. 2006; Fakhouri et al. 2010); and environmental processes (e.g. tidal stripping) alter subhalo structure (Hayashi et al. 2003; Peñarrubia et al. 2008; Errani & Peñarrubia 2020). Non-standard DM models (e.g. self-interacting or warm DM) predict systematically different internal structures (for example, core or cusp central density) and shapes (Rocha et al. 2013; Peter et al. 2013; Lovell et al. 2014; Tulin & Yu 2018; Sameie et al. 2018). Quantifying departures from self-similarity at the population level is therefore a sensitive test of galaxy formation physics and, in particular, of dark matter self-interactions through their impact on the shapes of galaxies.

Within the Milky Way, the combination of astrometric, photometric, and spectroscopic data, most notably from *Gaia* (Gaia Collaboration et al. 2018, 2021), SDSS (York et al. 2000), DES (Abbott et al. 2018), LAMOST (Cui et al. 2012) APOGEE (Majewski et al. 2017) and dedicated surveys, for example S^5 (Li et al. 2019), have enabled high precision, six-dimensional analyses of streams such as Palomar 5, GD-1, Sagittarius, and Orphan–Chenab (Koposov et al. 2010; Küpper et al. 2015; Bowden et al. 2015; Koposov et al. 2019; Malhan & Ibata 2019; Vasiliev et al. 2021; Koposov et al. 2023). These studies indicate a nearly spherical inner halo (Bovy et al. 2016; Palau & Miralda-Escudé 2023), while at larger radii the halo appears more flattened, triaxial, and potentially misaligned with the disk (e.g., Helmi & White 1999; Law & Majewski 2010; Vera-Ciro & Helmi 2013; Bonaca et al. 2014; Erkal et al. 2019; Vasiliev et al. 2021; Koposov et al. 2023; Nibauer & Bonaca 2025). The identification of gaps and spurs in GD-1 and Palomar 5 has further enabled tests of the predicted DM subhalo population on kiloparsec scales (Ibata et al. 2002; Carlberg et al. 2012; Erkal et al. 2016; de Boer et al. 2018; Bonaca et al. 2019; de Boer et al. 2020; Banik et al. 2021; Nibauer et al. 2025; Valluri et al. 2025), offering insights into the small-scale DM distribution and stream evolution in time-dependent potentials (e.g., Dillamore et al. 2022; Yavetz et al. 2023; Weerasooriya et al. 2025). Beyond the MW, M31’s Giant Southern Stream, spanning a wide range of galactocentric radii, has provided stringent constraints on its halo mass despite only semi-resolved photometric and spectroscopic stellar data (Fardal et al. 2013).

Extending stream analyses to more distant galaxies introduces observational and modelling challenges. Outside the Local Group, stars are unresolved and full six-dimensional phase-space information is generally unavailable, complicating proper motion, distance, and line-of-sight velocity measurements. Pioneering modelling of projected (two-dimensional; 2D) streams dates back to Johnston et al. (2001); since then, numerous studies have focused on low surface brightness (LSB), projected features with limited or no kinematic data (e.g., Tal et al. 2009; Martínez-Delgado et al. 2010; Mouhcine et al. 2010; Atkinson et al. 2013; Crnojević et al. 2016; Carlin et al. 2016; Hood et al. 2018; van Dokkum et al. 2019; Bflek et al. 2020; Sola et al. 2022; Martínez-Delgado et al. 2023; Yoon et al. 2024; Miró-Carretero et al. 2024; Sola et al. 2025). Amorisco et al. (2015)

fitted the projected surface brightness morphology of the NGC1097 “dog-leg” stream using the progenitor remnant’s line-of-sight velocity, enabling an estimate of the host’s halo mass. Pearson et al. (2022) analysed the Dw3 stream around Centaurus A using 2D positions and demonstrated a degeneracy between orbital velocity and halo mass. Incorporating even a single radial velocity measurement breaks this degeneracy and yields a lower bound on the host’s halo mass.

In many extragalactic systems, however, neither radial velocities nor distance gradients along the stream are available. Recent work shows that purely geometric diagnostics, such as stream track curvature and stream loop precession, still provide meaningful constraints on halo properties. Nibauer et al. (2023) demonstrated that curvature vectors of projected streams limit the orientation of the host’s acceleration field and thus constrain halo triaxiality. Complementarily, Walder et al. (2024) showed that multi-loop streams encode precession angles that inform halo radial structure, offering constraints on scale radii and concentrations without direct kinematics. In a more recent study, Nibauer & Pearson (2025) have leveraged a generative model for extragalactic stream to constrain the radial profile of the host potential. These methods highlight the untapped potential of photometric morphologies alone for probing DM halos.

Forthcoming wide-field imaging from the Rubin Observatory Legacy Survey of Space and Time (Rubin/LSST; Ivezić et al. 2019) and Euclid (Laureijs et al. 2011) will dramatically expand the census of streams around external galaxies (e.g., LSST Science Collaboration et al. 2009; Laureijs et al. 2011; Laine et al. 2018; Ivezić et al. 2019; Pearson et al. 2019, 2024; Walder et al. 2024). This increase in detections motivates population-level methodologies that combine information from multiple streams to deliver statistically powerful constraints on the distribution of halo properties across galaxies. Our approach is informed by the extensive stream-modelling literature in the MW (e.g., Johnston 1998; Binney 2008; Eyre & Binney 2011; Varghese et al. 2011; Küpper et al. 2012; Sanders & Binney 2013; Gibbons et al. 2014; Sanders 2014; Bovy 2014; Bowden et al. 2015; Fardal et al. 2015; Amorisco 2015; Hendel & Johnston 2015; Erkal et al. 2019) and recent advances for external galaxies (e.g., Pearson et al. 2022; Nibauer et al. 2023; Walder et al. 2024).

In contrast to previous studies which considered fits to individual streams, we leverage hierarchical modelling to combine multiple low informative fits and obtain strong population level constraints on halo shape distributions.

In this study, we present a population based framework for analysing extragalactic stellar streams. We validate an end-to-end pipeline on simulations by fitting streams for individual systems and then performing hierarchical Bayesian inference to constrain the distribution of DM halo shapes across a galaxy population. To do so, we have developed **StreaMAX** (a, a novel, publicly available, Python package to rapidly model streams leveraging JAX (Bradbury et al. 2018), a high-performance numerical computing library with automatic differentiation and just-in-time (JIT) compilation. It enables efficient computation on CPUs, GPUs, and TPUs, making it especially useful for optimization and Bayesian inference.

This work serves as a proof of concept and therefore relies exclusively on simulated data. In a following companion paper, we will apply our method to real observations. However, while several catalogues of stellar streams already exist, their depth, processing, and feature definitions vary significantly, and most identified structures are unsuitable for our modelling framework either being too short, too straight, or too disturbed by major mergers. To overcome this, we introduced in a companion paper the STRINGS sample (Sola et al. 2025), a catalogue of 35 nearby galaxies hosting long, faint, and curved streams, selected for their suitability for dynamical

modelling. Using residual images from the DESI Legacy Imaging Surveys (DESI-LS, [Dey et al. \(2019\)](#)), which enhance faint features by modelling and subtracting all bright sources, we visually inspected thousands of galaxies and segmented streams meeting our criteria. The resulting sample provides high quality, well defined stream tracks ideal for forward modelling. In future work currently underway, we will apply the methodology developed here directly to STRINGS to infer the population-level distribution of dark matter halo shapes across galaxies in the Local Universe.

The paper is organised as follows. Section 2 describes the stream-generation and forward-modelling methodology. Section 3 presents the fitting procedure for individual simulated streams. Section 4 outlines the hierarchical Bayesian model and reports population-level constraints on halo shapes. Section 5 summarises our discussions and conclusions.

2 METHODS

This work aims to infer the morphology of dark matter haloes from extragalactic stellar streams with no kinematic information. To achieve this, we first construct a three-dimensional model of a tidal stream evolving in a given gravitational potential, which is then projected onto the plane of the sky. From this projection, we extract the stream’s track defined as a one-dimensional ridgeline, an idealised, widthless trajectory tracing its central path. The parameters governing this forward-modelling pipeline will be described at the end of this section, along with the physically motivated priors adopted to limit degeneracies, constrain modalities, and ensure observational realism.

2.1 Stream Generation

A variety of methods exist to generate stellar streams, trading realism for computational cost. The most straightforward approximation, treating stream tracks as orbits (e.g. [Koposov et al. 2010; Malhan & Ibata 2019](#)), is known to be biased ([Sanders & Binney 2013](#)). Early work therefore used orbit fits with corrective terms ([Varghese et al. 2011](#)), followed by test-particle, streakline, or particle-spray techniques that more faithfully capture leading and trailing tails ([Küpper et al. 2012; Gibbons et al. 2014](#)). N -body simulations best model disruption and self-gravity but are orders of magnitude more computationally expensive, as each particle interacts with every other one ([Eyre & Binney 2011; Sanders 2014](#)). Here we adopt the particle-spray method (e.g. [Johnston 1998; Küpper et al. 2012; Gibbons et al. 2014; Fardal et al. 2015](#)), which has been shown to accurately and efficiently reproduce stream tracks.

In our implementation, the progenitor is modelled as a simple analytic potential, a Plummer sphere, specified by a characteristic mass and scale radius. This analytic form provides a smooth, time-independent description of the progenitor’s self-gravity, which is required both to compute its tidal boundary and to determine the characteristic scale of the escaping debris. Rather than follow the evolution of all stars bound to the progenitor, we assume that only particles escaping through the tidal Lagrange points contribute materially to the observable stream. This avoids integrating large numbers of particles that would remain bound and never enter the debris.

At each integration step we therefore compute the instantaneous inner (L1) and outer (L2) Lagrange points. These are the saddle points of the effective potential along the line joining the Galactic centre to the progenitor, determined by the balance between the host’s gravitational field, the progenitor’s self-gravity, and the centrifugal

term in the co-rotating frame ([King 1962](#)). They define the two primary escape channels through which material becomes unbound during tidal stripping.

New debris particles are *sprayed* from small spatial and velocity offsets around L1 and L2. These offsets serve as a proxy for the progenitor’s internal velocity dispersion and naturally generate both leading and trailing arms. In this work we adopt the dispersion prescription of [Fardal et al. \(2015\)](#), which samples position and velocity perturbations consistent with the Plummer model and produces cold, kinematically coherent streams. Because we inject particles only at the tidal boundary, every spawned tracer is, by construction, likely to escape the progenitor rather than remain bound.

Once released, particles are treated as massless tracers and evolved forward in time under the combined gravitational field of the host potential and the progenitor’s analytic potential. The progenitor therefore continues to influence nearby debris until the particles move several scale radii away, at which point its contribution becomes negligible. Crucially, the debris particles do not exert forces on one another, which eliminates the $\mathcal{O}(N^2)$ scaling of full N -body simulations and enables extremely fast generation of realistic streams. Despite this simplification, the particle-spray method reproduces key morphological features of tidal streams such as bifurcations, arm asymmetries, and on-sky track curvature with excellent fidelity and at orders-of-magnitude lower computational cost compared to full N -body simulations (e.g. [Sanders et al. 2016; Chen et al. 2025](#)). Even so, a single spray realisation typically requires a few seconds, making large fitting campaigns (hundreds of thousands of streams) computationally heavy.

To address this, we built [StreaMAX](#) , a fully JAX ([Bradbury et al. 2018](#))—accelerated package that exactly reproduces conventional spray generators, such as the ones in [GALA](#) ([Price-Whelan 2017](#)) and [AGAMA](#) ([Vasiliev 2019](#)), while gaining orders of magnitude of speed-up through compilation and efficient parallelism. Crucially, spray particles evolve independently, meaning that every particle can be integrated in parallel without requiring any information on any other particle. Therefore, we can accelerate the time integration using vectorised mapping and Just-in-Time (JIT) compilation. The whole package is written in JAX meaning that gradients of any function can easily be obtained.

Figure 1 shows the time required to generate a stream as a function of the number of particles. All pipelines are tested using identical stream parameters and orbital integration settings. Note that [Agama](#) was excluded from the comparison because it uses a different integration algorithm which can not be changed. CPU benchmarks were performed on a 44-core node, and GPU results use an NVIDIA L4. On the CPU, [Gala](#) and [StreaMAX](#) exhibit similar scaling with particle number, with [StreaMAX](#) being the fastest across all tested sizes. When run on a GPU, [StreaMAX](#) achieves a substantial speedup and displays a flat scaling curve for low number of particles and a slight trend upwards at higher values. This suggests that fixed overheads dominate for low sizes where adding particles barely affects runtime. Although GPUs provide the best performance, our main analyses use CPUs due to wider availability on our computing resources. Throughout this work, we generate streams with 10^4 particles.

The time integrations are performed using a standard leapfrog scheme ([Hockney & Eastwood 1988](#)) with fixed time steps. In this work, since the assumed potential model is smooth and well behaved (see Subsection 2.3), the number of steps is set to 100. This choice was empirically tested and shown to conserve energy and yield negligible differences compared to integrations with substantially smaller time steps. For more efficient computing, we want to have the same amount of total steps taken for every particle but, in the spray method,

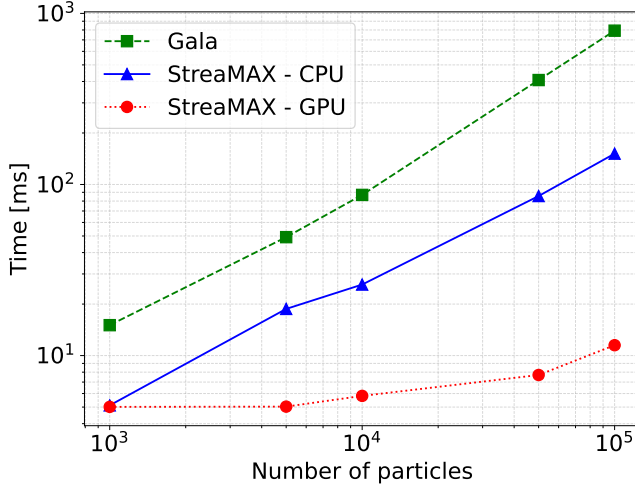


Figure 1. Time required to model a tidal stream as a function of the number of particles, using identical integration settings across *Gala* and *StreaMAX* on both CPU and GPU. CPU tests were performed on a 44-core node, and GPU tests use an NVIDIA L4. *StreaMAX* outperforms the conventional package, with the GPU version delivering the fastest and flattest scaling with particle number.

particles are born at different times. A particle released later has less total time to evolve, so its timestep must be smaller if it is still to take the same number of steps as earlier particles. In practice, this means early-born particles have larger timesteps and late-born particles have smaller ones. For efficient vectorisation and JIT compilation, JAX requires fixed array dimensions, which motivates adapting the temporal resolution as a function of integration time for each particle.

2.2 Track Extraction

As mentioned earlier, streams are generated in 3D, then projected onto the sky. Because the potential's orientation is already a sampled parameter (see Section 2.3), varying the viewing direction (i.e., the line of sight from which the stream is projected) is unnecessary; a fixed projection suffices. Here, for simplicity, we choose the XY -plane. Note that the progenitor's final phase-space coordinates are free parameters in the inference, so the stream's orbital plane is not fixed and can vary relative to the line of sight even under a fixed projection choice. In this paper we fit only the stream track, intentionally discarding width and density information.

To extract the track from a modelled stream, we need to obtain the ordering of the particles along the stream. To do so, we unwrap each particle's orbital angle individually. We begin by integrating the full 3D orbit of the progenitor. Because this orbit is continuous, the ordering of points along it is already known, and its angular coordinate can be unwrapped in the usual sense (i.e., allowing the angle to increase beyond 2π rather than resetting after each revolution). We then use the progenitor's unwrapped angle to assign a birth angle to each stream particle. Since particles are released at different times, their true initial angle is not restricted to the interval $[0, 2\pi]$. Instead, the initial angle of a particle is defined as the progenitor's unwrapped angle at the particle's birth time, plus the particle's own phase offset within $[0, 2\pi]$. Finally, we re-centre all particle angles by subtracting the progenitor's final unwrapped angle. With this convention, trailing-tail particles have negative angles, the progenitor sits at 0° , and leading-tail particles have positive angles. This procedure assumes

monotonically increasing angles along each orbit and works robustly for our setups.

We extract the stream track by binning azimuthally the unwrapped angular coordinate and averaging the particle radii within each bin. This procedure follows the method of [Sola et al. \(2025\)](#), where we used it to automatically extract the tracks of segmented real external streams (see their Figure B1). The key improvement here is that our ordering and binning are fully automated, requiring no human intervention and thus enabling population-scale inference. The same bins can also provide estimates of the stream density (particle counts) and width (radial standard deviation), but these quantities are not used in the present work because our current particle-spray prescription does not produce realistic density and width profiles. This is because (i) the progenitor mass is held constant throughout the disruption, and (ii) particles are released from the Lagrange points at uniform time intervals, independent of their separation from the progenitor. Therefore, we choose to work using only the stream track which retains geometric information about the global potential shape but loses dynamical information about the progenitor mass, disruption history, and local potential fluctuations ([Bonaca & Hogg 2018](#)).

In this work, the angular bin size is fixed at 10° . This choice, adopted from [Sola et al. \(2025\)](#), represents a balance between maximising angular resolution and maintaining sufficient information per bin to limit radial uncertainties. In *STRINGS*, this binning led to an average radial distance uncertainty of approximately 2% which we include as Gaussian radial noise in our mock data.

2.3 Model Parameters

Before introducing our model parameters, we note that in this work the potential used to generate the mock streams is the same as the potential assumed during modelling. This choice is not required in general, but it allows us to test the intrinsic constraining power of our pipeline without introducing additional bias from mismatches between model and data.

We model streams in an axisymmetric Navarro-Frenk-White (NFW) potential. The halo is characterised by its mass M_{halo} , scale radius R_s , an axis ratio (flattening in the density) q , and the orientation of the flattened axis, represented by a vector $\mathbf{r} = (\hat{x}, \hat{y}, \hat{z})$. The stream progenitor is a Plummer sphere with mass m_{prog} and scale radius r_s . To backward integrate, we need its final (present-day) phase-space coordinates: $(x_0, y_0, z_0, v_{x0}, v_{y0}, v_{z0})$. We also specify the total integration time t_{int} . The origin is fixed at the halo centre and is not allowed to vary. This gives a total of fifteen parameters needed to model a stream. A schematic is shown in Figure 2.

Although an axisymmetric potential can be specified with two orientation angles, sampling angles directly is prone to multimodality: periodic boundaries imply that a true solution near 0 (or 2π) induces duplicate modes at both ends of the parameter space. Instead, we parametrise the orientation of an axisymmetric halo by a nonzero vector

$$\mathbf{r} = (\hat{x}, \hat{y}, \hat{z}) \in \mathbb{R}^3. \quad (1)$$

In the prior, we draw

$$\hat{x}, \hat{y}, \hat{z} \sim \mathcal{N}(0, 1), \quad (2)$$

independently, and define the auxiliary radius

$$r = \|\mathbf{r}\| = \sqrt{\hat{x}^2 + \hat{y}^2 + \hat{z}^2} > 0. \quad (3)$$

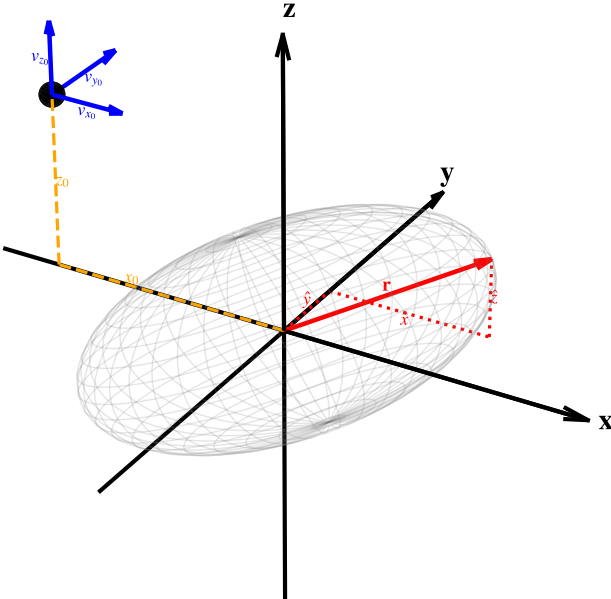


Figure 2. Schematic representation showing the coordinate system of the axisymmetric NFW potential (grey grid), the halo flattened axis r , and the progenitor's present-day phase-space location (black circle). The origin is fixed and taken as the centre of the DM halo.

The direction of the halo symmetry axis is then given by the unit vector

$$\hat{n} = \frac{r}{r}. \quad (4)$$

To remove the trivial reflection degeneracy of an axisymmetric potential we impose

$$\hat{n}_z \geq 0, \quad (5)$$

which restricts the prior support to one hemisphere. Because the prior is spherically symmetric, this induces an isotropic prior over orientations while avoiding angular periodicity. Mathematically, the only remaining degeneracy in this parametrisation occurs on the boundary $n_z = 0$, where opposite directions of \hat{n} (e.g. $(1, 0, 0)$ and $(-1, 0, 0)$) correspond to the same physical model but appear as distinct points in parameter space.

Since we only use the orientation of \mathbf{r} , its scale is redundant and introduces a new degeneracy where every combination of $(\hat{x}, \hat{y}, \hat{z})$ with the same orientation but different magnitude generate the same stream. To fix that, we use the magnitude r (length of the vector \mathbf{r}) to define the halo flattening q . The goal is to transform \mathbf{r} into a uniform distribution on $[q_{\min}, q_{\max}]$.

Since r is multivariate normal with zero mean and unit covariance, the radius r follows the Maxwell distribution with unit scale. Its probability density function (pdf), f_R , and cumulative distribution function (cdf), F_R , are

$$f_R(r) = \sqrt{\frac{2}{\pi}} r^2 \exp\left(-\frac{r^2}{2}\right), \quad r \geq 0, \quad (6)$$

$$F_R(r) = \int_0^r f_R(s) \, ds = \operatorname{erf}\left(\frac{r}{\sqrt{2}}\right) - \sqrt{\frac{2}{\pi}} r \exp\left(-\frac{r^2}{2}\right), \quad (7)$$

where erf is the error function and F_R is strictly increasing from 0 to 1 on $[0, \infty]$. We introduce an intermediate variable

$$u = F_R(r), \quad (8)$$

which by the probability integral transform satisfies

$$u \sim \mathcal{U}(0, 1), \quad (9)$$

independently of the orientation $\hat{\mathbf{n}}$.

We then define the physical halo flattening q by an affine mapping

$$q = q_{\min} + (q_{\max} - q_{\min}) u, \quad (10)$$

with fixed bounds $q_{\min} < q_{\max}$. Since u is uniform on $[0, 1]$, q is exactly uniform on $[q_{\min}, q_{\max}]$. In this work, we choose $q_{\min} = 0.5$ and $q_{\max} = 1.5$ to obtain a uniform prior $q \in [0.5, 1.5]$, centred on spherical ($q = 1$) with equal prior weight for oblate ($q < 1$) and prolate ($q > 1$).

In terms of the radius r , the flattening is therefore

$$q(r) = q_{\min} + (q_{\max} - q_{\min}) \left[\operatorname{erf}\left(\frac{r}{\sqrt{2}}\right) - \sqrt{\frac{2}{\pi}} r \exp\left(-\frac{r^2}{2}\right) \right]. \quad (11)$$

This parametrisation yields:

- (i) an isotropic prior over halo orientations $\hat{\mathbf{n}}$ (restricted to $\hat{n}_z \geq 0$), and
- (ii) an exactly uniform prior over the flattening a on $[a_{\min}, a_{\max}]$.

while avoiding angular periodicity and any arbitrary normalisation of r . From Equation 11, the q_{\min} boundary corresponds to the single point $r = 0$, which may appear problematic, however, this has no practical consequence because the intermediate variable u is explicitly rescaled to be uniform on $[0, 1]$.

We, also, impose constraints on the progenitor’s final conditions. The observer is always fixed at $+z$ -axis, so that the plane of the sky corresponds to the XY plane. First, we fix $y_0 = 0$, which forces the progenitor’s final position to lie in the XZ plane, regardless of any other parameters. This assumes we know the progenitor’s position in one dimension, an assumption that does not always hold. However, in our mock data, the stream contains no width or surface-density information, so the progenitor’s on-track location is far less constrained and more easily shift freely along the stream. To avoid this degeneracy, we fix one dimension of the progenitor’s final position rather than treat it as a parameter to be inferred. This choice simplifies the modelling problem but removes our ability to test constraints that depend on the progenitor’s present-day location, such as its intrinsic parameters, orbital precession, or aspects of the host’s radial structure (e.g. [Belokurov et al. 2014](#); [Erkal et al. 2016](#); [Bonaca & Hogg 2018](#)). Although the progenitor’s position can sometimes be constrained from the track alone, we found that, without width or density information, doing so offers little additional benefit for our mock setup and therefore chose not to model it as a free parameter. In addition, we require $x_0 > 0$, $z_0 > 0$, and $v_{y_0} > 0$. The constraint on x_0 simply fixes the in-plane orientation of the track; $z_0 > 0$ breaks the front/back degeneracy of projection; and $v_{y_0} > 0$ assumes leading and trailing tails are interchangeable which is reasonable at low resolution where unresolved stars do not reveal the local “S”-shape near the progenitor ([Choi et al. 2007](#)). From our tests, these assumptions do not affect the recovered posteriors of the halo parameters but greatly speed up the inference by cutting away modalities.

Table 1. Priors for the thirteenth inferred parameters. $\mathcal{U}(a, b)$ denotes a uniform prior on $[a, b]$; $\mathcal{N}(\mu, \sigma)$ denotes a Gaussian prior with mean μ and standard deviation σ . Inequality constraints implement the symmetry-breaking choices described in the text.

Parameter	Symbol	Prior	Units
Halo mass	$\log_{10}(M)$	$\mathcal{U}(11, 14)$	$\log_{10}(M_\odot)$
Halo scale radius	R_s	$\mathcal{U}(10, 25)$	kpc
Halo orientation and shape	$\hat{x}, \hat{y}, \hat{z}$	$\mathcal{N}(0, 1)$ with $\hat{z} \geq 0$	–
Progenitor mass	$\log_{10}(m)$	$\mathcal{U}(7, 9)$	$\log_{10}(M_\odot)$
Progenitor scale radius	r_s	$\mathcal{U}(1, 5)$	kpc
Final positions	x_0, z_0	$\mathcal{N}(0, 150)$ with $x_0 > 0, z_0 > 0$	kpc
Final velocities	$v_{x_0}, v_{y_0}, v_{z_0}$	$\mathcal{N}(0, 250)$ with $v_{y_0} > 0$	km s^{-1}
Integration time	$time$	$\mathcal{U}(1, 4)$	Gyr

After applying the above symmetries, we infer a total of thirteen parameters summarised in Table 1. The priors are physically motivated but deliberately chosen to be wide and weakly informative. Halo and progenitor masses are given log-uniform priors; scale radii are uniform on broad ranges. We sample progenitor masses in the dwarf galaxy regime because we focus on external streams, where globular cluster streams are unlikely to be detectable. Although globular clusters and dwarf galaxies overlap in stellar mass, where globular clusters typically span 10^5 – $10^7 M_\odot$ (e.g. Harris 1996, 2010), while classical dwarf galaxies range from 10^6 – $10^9 M_\odot$ (McConnachie 2012), their tidal debris differ significantly in surface brightness and width. For this reason, we restrict our progenitor mass sampling to the massive dwarf galaxy range. As mentioned above, the halo-axis components $\hat{x}, \hat{y}, \hat{z}$ have independent Gaussian priors (with $\hat{z} \geq 0$), while the flattening q is deterministically mapped to a uniform prior [0.5, 1.5]. The present-day positions and velocities of the the progenitor are also sampled from Gaussians, in some cases, the prior is truncated based on the restriction mentioned earlier. This ensures isotropy and limits degeneracies. The integration time is uniform. The lower bound of 1 Gyr, though arbitrary, allows sufficient time for streams to form, while the upper bound of 4 Gyr represents the timescale beyond which streams are expected to have phase-mixed enough to no longer be observable (e.g. Mancillas et al. 2019). Throughout the modelling, we generate each stream using 10,000 particles. In this work, our main target is q ; we also constrain in the orientation of the halo but all the remaining parameters are considered nuisance variables required to generate the track.

Lastly, to ensure that the mock data generated is both observationally realistic and sufficiently informative to warrant modelling, we generate mock observations by selecting projected tracks that meet three criteria: (i) angular coverage $> \pi/2$, (ii) arc length > 100 kpc and (iii) radial extent within [10, 500] kpc. These conditions roughly line up to the STRINGS sample (Sola et al. 2025). The first two ensure broad angle and spatial coverage; the third keeps the stream far enough from the bright host to be observed but close enough to be affected by the halo. For robustness, an angle bin is included in the mock data only if it contains ≥ 100 particles, whereas during fitting we allow a lower threshold (half as many) to avoid discarding acceptable realisations due to stochastic particle losses. This minimum threshold on the amount of particles per bin also reflects the fact that only dense enough regions of the stream will be detected, and thus modeled.

3 INDIVIDUAL FIT

Our goal is to simultaneously obtain, for each mock track, the posterior of the halo flattening q and orientation for an axisymmetric NFW potential by leveraging Bayesian inference. Recall that q is a

deterministic function of the length of the sampled orientation vector $(\hat{x}, \hat{y}, \hat{z})$ (Equation 11). All remaining parameters are treated as nuisance variables required to generate the stream. In Section 4 we combine the marginal posteriors of q from many streams to infer the DM haloes parameters at a population level.

3.1 Likelihood

We begin by fitting each mock track individually. For this, we employ a Bayesian inference approach grounded in Bayes’ theorem (Bayes & Price 1763). Let D denote the data associated with a single stream (e.g. binned radii as a function of angle), and let θ denote the corresponding model parameters. We assume a specified forward model M that maps θ to predicted observables. Bayes’ theorem for continuous parameters reads

$$p(\theta|D, M) = \frac{p(D|\theta, M) \pi(\theta|M)}{Z(M)}, \quad (12)$$

where:

- $p(\theta|D, M)$ is the posterior density,
- $\pi(\theta|M)$ is the prior density on θ given model M ,
- $p(D|\theta, M)$ is the likelihood, and
-

$$Z(M) = p(D|M) = \int p(D|\theta, M) \pi(\theta|M) d\theta \quad (13)$$

is the evidence (marginal likelihood).

In what follows we keep M fixed and write $p(D|\theta)$ for brevity. Since we are not performing a model comparison, we drop the evidence term and work with the proportional form. For the inference, we adopt the same wide, weakly informative priors used in data generation (Table 1), but without the three selection cuts used to define mock-observation quality.

We assume that the observed projected track is binned in an angular coordinate ϕ , yielding N bins at angles $\{\phi_i\}_{i=1}^N$. In each bin we observe a projected radius r_i^{data} with an associated radial uncertainty $\sigma_i > 0$. The forward model M predicts, for a given θ , corresponding radii $r_i^{\text{model}}(\theta)$ at the same angles.

We adopt a Gaussian noise model in radius:

$$r_i^{\text{data}} \sim \mathcal{N}\left(r_i^{\text{model}}(\theta), \sigma_i^2\right), \quad i = 1, \dots, N, \quad (14)$$

with the bins conditionally independent given θ . This yields the likelihood

$$p(D|\theta) = \prod_{i=1}^N \frac{1}{\sqrt{2\pi} \sigma_i} \exp\left[-\frac{1}{2} \left(\frac{r_i^{\text{data}} - r_i^{\text{model}}(\theta)}{\sigma_i}\right)^2\right]. \quad (15)$$

For numerical work, we maximise or sample from the log-likelihood

$$\log p(D|\theta) = -\frac{1}{2} \sum_{i=1}^N \left[\left(\frac{r_i^{\text{model}}(\theta) - r_i^{\text{data}}}{\sigma_i} \right)^2 + \log(2\pi\sigma_i^2) \right]. \quad (16)$$

In the specific mock setup considered, each σ_i is taken to be a fixed fraction of the observed radius,

$$\sigma_i = \beta r_i^{\text{data}}, \quad (17)$$

with β a constant. Here, as mentioned in Section 2.2, we added a 2%

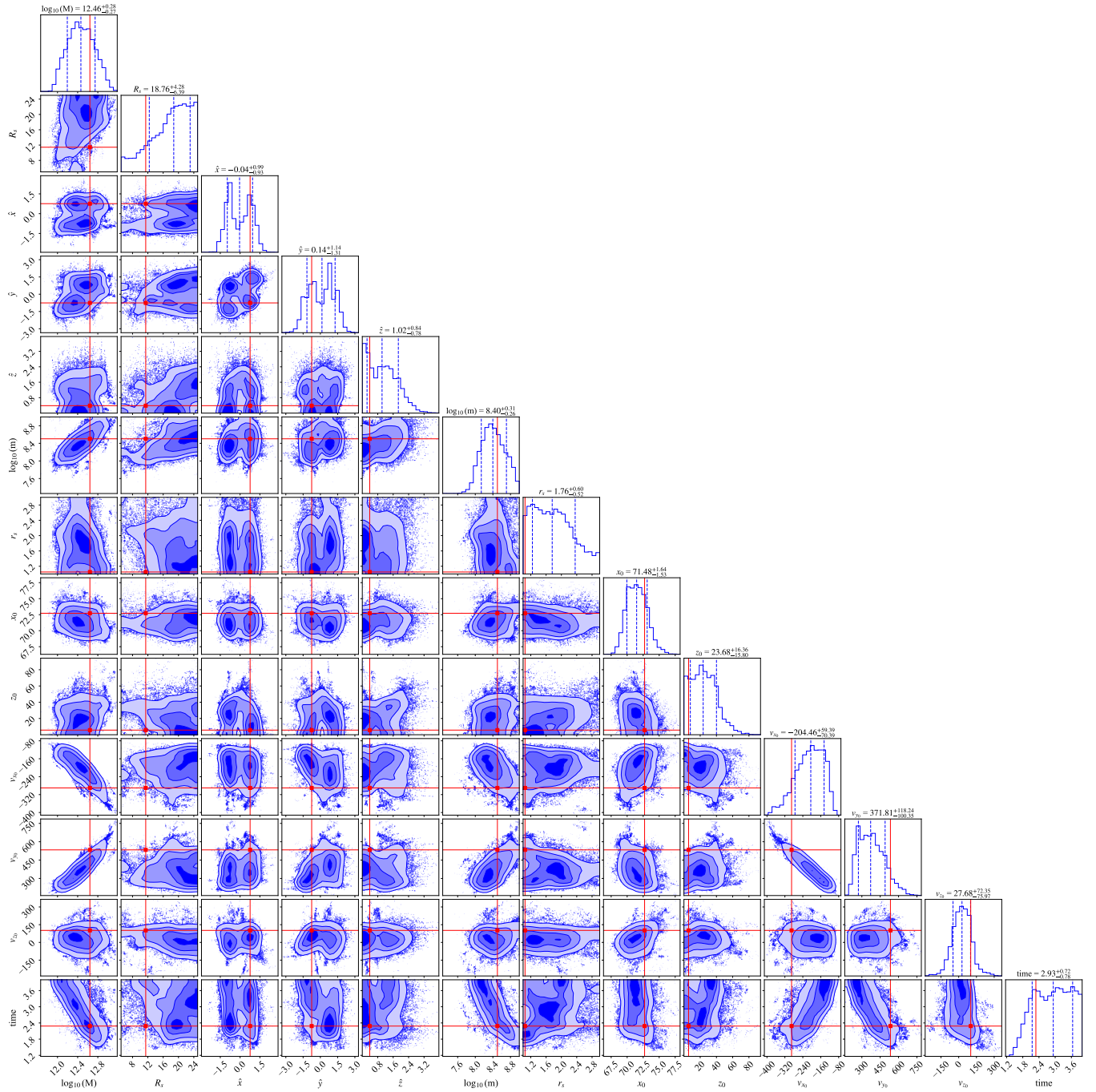


Figure 3. Corner plot for a single projected stream fit (13 parameters). Posteriors are shown in blue and the ground truth in red. The mock data include 2% Gaussian radial noise. Overall, the posteriors recover the truth, though several degeneracies remain (see Section 3.3).

Gaussian noise to the radius of the mock data based on STRRINGS (Sola et al. 2025). Therefore, for our Gaussian likelihood to be correct and completely unbiased, we set $\beta = 0.02$.

Models that do not cover all angular bins present in the data (for example, if the modelled track is too short in ϕ) can either be discarded, $\log p(D|\theta) = -\infty$ for such θ , or penalised by adding an explicit term to Eq. (16). For instance, if $\Delta\phi_{\text{data}}$ is the total angular extent of the data and $\Delta\phi_{\text{overlap}}(\theta)$ is the angular overlap of the model on the data, one possible penalty is

$$\log p_{\text{eff}}(D \mid \theta) = \log p(D \mid \theta) - \lambda \left[1 - \frac{\Delta\phi_{\text{overlap}}(\theta)}{\Delta\phi_{\text{data}}} \right]_+^2 \quad (18)$$

where $[x]_+ = \max(x, 0)$ and $\lambda > 0$ is a tunable constant. In the main text of a results paper one should specify whether a hard rejection or an explicit penalty of the form (18) is used. For this work, if the model's angular extent does not cover the data, we discard it, and if it extends beyond the range of the data, no penalty is applied. This reflects the assumption that limited observational coverage does not

rule out intrinsically longer tracks. Indeed, we can only detect the portion of a stream that is bright enough to rise above the surface brightness limit of a given survey. Therefore, the fainter parts of a stream may remain undetected, even if the stream physically extends into those regions.

Given the dimensionality and complex posteriors, we use dynamic nested sampling with Dynesty (Higson et al. 2019; Speagle 2020; Koposov et al. 2022), starting from 2000 live points and using the *rslice* sampler. Typical single-stream fits on an 80-thread CPU take ~ 10 hours.

3.2 Parameter Inference

Figure 3 presents the full 13-parameter corner plot for one mock track. Despite our prior constraints and parameterisation choices, several degeneracies persist (see Section 3.3). Nevertheless, most posteriors align well with the ground truth (red). Recall that all parameters except the halo flattening q are treated as nuisance parameters. The orientation components $(\hat{x}, \hat{y}, \hat{z})$, from which q is deterministically obtained, are comparatively well constrained, though they exhibit multi-modality among themselves. Importantly, they show no strong degeneracy with the remaining parameters (see Section 3.4 for some examples of flattening posteriors).

A notable feature is the marginalised posterior of the integration time. Low values are disfavoured up to ~ 2 Gyr, beyond which the posterior becomes broadly flat. This is a by-product of our conservative likelihood design: model tracks that are shorter than the observed angular coverage incur a strong penalty, whereas longer tracks are not penalised. As a result, the sampler is biased toward longer integration times, and once the integration time is sufficiently large for the model to span the observed range, the posterior plateaus. We discuss time-related degeneracies in Section 3.3, but note here that this behaviour is driven by the likelihood construction rather than by information in the data.

To validate the fits, we draw 1000 posterior samples at random and overlay their modelled tracks on the mock observations in Figure 4. The full posterior typically contains hundreds of millions of samples, but we downsample to not have to remodel all these tracks. Note that because the 1000 samples are selected uniformly at random, the displayed distribution is representative of the full posterior. The modelled tracks align closely with the data. Deviations are larger toward the ends of the tails, where fewer particles are present, leading to increased model deviation. The residuals (right panel), computed as data minus model in the radius-angle space where the likelihood is evaluated, show no obvious systematic bias. Together, these checks confirm that the inferred models are consistent with the mock data.

3.3 Degeneracies

In this work we fit only the projected track of modelled streams, with no velocity information. As shown by Pearson et al. (2022), this implies a fundamental scale degeneracy between orbital velocity and halo mass: without kinematics it is not possible to fix the physical mass scale of the system. To visualise these relations we compute the present-day velocity $v = \sqrt{v_{x0}^2 + v_{y0}^2 + v_{z0}^2}$ and examine the correlations between $\{\log_{10}(M), \log_{10}(m), \log_{10}(v), \text{time}\}$ (Figure 5). Because $v^2 \propto M$, $\log_{10}(M)$ and $\log_{10}(v)$ are linearly correlated in log–log space. A second linear relation between $\log_{10}(M)$ and $\log_{10}(m)$ arises from the Lagrange-point scaling. In the rotating frame of the progenitor, the tidal radius r_t is set by the balance between the progenitor’s self-gravity and the tidal force exerted by

the host: $r_t \propto (\frac{m}{M})^{\frac{1}{3}}$. If m and M are scaled proportionally, the ratio m/M remains constant, and therefore the tidal radius (i.e. the location of the Lagrange points where particles are released) remains unchanged. Since our stream generation method releases debris precisely from these Lagrange points, a fixed r_t produces an identical phase-space structure. The resulting streams are thus completely degenerate as long as M/m is held constant. In logarithmic units, keeping this ratio fixed corresponds to a linear relation between $\log_{10}(M)$ and $\log_{10}(m)$. Finally, the integration time trades off against the mass–velocity scale: if (M, v) are scaled down, a longer integration time is required to match the observed length and vice-versa. From the inferred joint posteriors in Figure 5, we see that although the parameters are strongly degenerate, the ground truth lies directly along the degeneracy. When looking only at the marginalized posteriors (Figure 3), these parameters may appear well constrained. However, we stress that such constraints are prior-driven: likelihood values are nearly constant along the degeneracy, but the prior does not weight all regions equally, producing apparent preferences in the marginal distributions. Uniform priors on the parameters do not guarantee uniform priors on the degeneracies. In principle, one could reparameterise the problem to uniformly sample along the degeneracies; in practice, because enclosed mass varies with radius, the exact mass–velocity relation is position dependent. We therefore retain the raw parameters and explicitly note that these apparent constraints are prior dominated.

Figure 3 also reveals clear modalities between the different orientations that propagate to the flattening. Figure 6 zooms in on the (\hat{x}, \hat{y}) posterior, showing four modes. For each mode we plot the best-fit stream with the rainbow colormap colour-coding the ordering of the stream particles over the mock data (red) and the projected equipotentials; the corresponding flattening q is listed atop each panel. All four solutions fit the data and share nearly the same projected potential even though (\hat{x}, \hat{y}) and q differ. Looking at the two pairs, green-purple and red-orange, we see that in both cases the flattening is the same, either oblate or prolate. In the posterior, the modalities are equivalent to flipping the sign of both \hat{x} and \hat{y} which, in the projected plane, represents a simple 180° rotation. These modalities are due to the loss of information from working with projections. Indeed, the potentials’ orientations are different in 3-dimensions but look similar when projected. Other posterior pairs, for example the green and orange solutions, differ in both orientation and flattening, yet still produce nearly identical projected tracks. In these cases, the inferred orientation flips the sign of \hat{x} while \hat{y} remains similar, which corresponds to a $\sim 90^\circ$ rotation of the halo in the projected plane. Combined with the change from an oblate ($q = 0.86$) to a prolate ($q = 1.46$) configuration, this transformation yields similar projected potentials. As a result, both 3D models fit the 2D data almost equally well. This demonstrates that when the projected potential matches the ground truth, distinct posterior modalities can appear. That being said, these modes are not perfect. Our results show that the correct solution is nonetheless favoured. This reinforces the idea that even in projection, stream tracks carry information about the underlying three dimensional potential. This phenomenon is in agreement with the results presented in Nibauer et al. (2023) showing that the projected curvature allows to constrain the morphology of the halo’s potential. Notably, the best fit streams in Figure 6 differ in the regions not covered by the mock data, suggesting that longer streams (i.e. wider angular coverage) could help break this degeneracy. We return to these points in more detail in Section 3.4.

Lastly, looking back at Figure 3, we see in the marginalized posterior of \hat{z} two modes. Here, these modalities mostly dictated the length

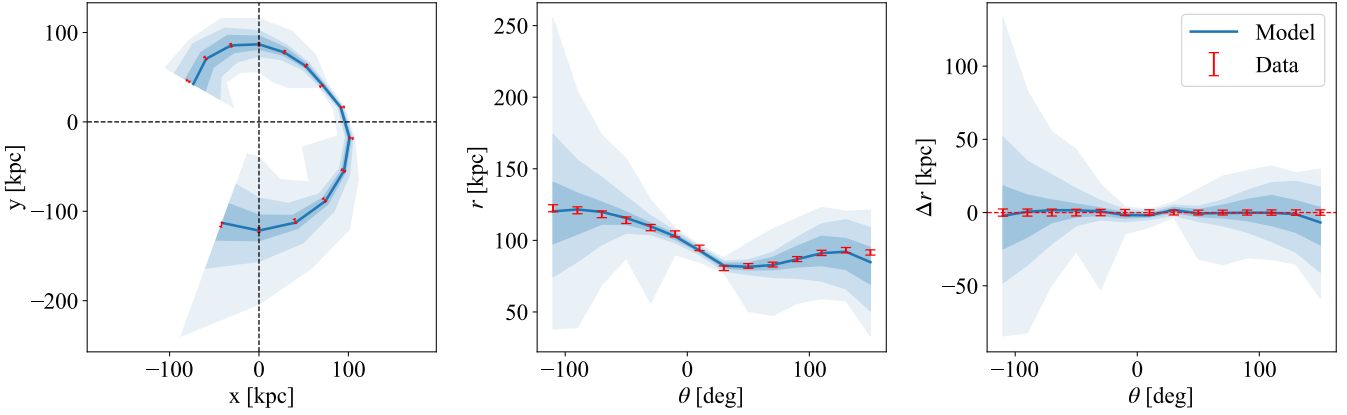


Figure 4. Summary of the 1000 samples drawn uniformly at random from the posterior (blue) compared to the ground truth (red) for a single stream. Shading indicates the $1, 2$, and 3σ drawn sample envelopes. **Left:** Comparison between the samples to the mock data on the XY plane. **Middle:** Same comparison in the radial distance versus angle plan, where the likelihood is evaluated as the radial difference at fixed angle bins. **Right:** Radius residuals (data minus model) as a function of angle. Fits track the mock data well; larger deviations near the ends of the stream reflect lower particle counts and increased sampling noise. Residuals show no obvious bias.

of the vector (see Equation 11) which maps to the flattening, allowing to vary the potential from oblate to prolate without affecting the projected orientation in the XY plane. This is how pairs of different flattening in Figure 6 obtain different values for q without varying the absolute size of \hat{x} and \hat{y} .

Although the three-dimensional components defining the DM halo orientation ($\hat{x}, \hat{y}, \hat{z}$) are highly degenerate with one another, Figure 3 shows that the projected orientation is nonetheless well constrained. While this aspect is not explored further in the present work, such constraints could be compared to the observed orientation of the baryonic components in real galaxies, allowing the misalignment between the stellar (or stellar + gaseous) disk and the DM halo to be quantified statistically (e.g. [Bailin & Steinmetz 2005](#); [Bett et al. 2010](#); [Debattista et al. 2013](#); [Shao et al. 2016](#); [Tenneti et al. 2016](#)). Measuring this misalignment across a large sample, which we are currently doing with STRINGS, enables to study the population-level relationship between halo and disk orientations. Moreover, the inferred sky-projected orientations could be analysed to test whether haloes are randomly distributed or exhibit coherent alignments tracing the surrounding large-scale structure, as suggested by studies of the cosmic web (e.g. [Tempel & Libeskind 2013](#); [Codis et al. 2015](#); [Welker et al. 2020](#)).

3.4 Flattening

We now run our inference pipeline for three different cases: ground truth oblate, spherical and prolate. With posteriors on $(\hat{x}, \hat{y}, \hat{z})$ from three different individual fits derived in Section 3.2, we obtain the halo flattening using Equation 11. Figure 7 shows the three examples respectively from left to right, each with the best-fit stream (top) and the corresponding posterior for q (bottom). The ground truths are marked in red. In all cases the fits match the mock data well and the q posteriors favour the correct values. For the spherical case, extreme oblate or prolate solutions are ruled out and the posterior peaks tightly at $q \simeq 1$. For the oblate case, no value of q is completely ruled out but the correct value is preferred. This is not always true for all oblate cases. Lastly, the prolate case also does not completely rule out any flattening possibility but does exhibit a secondary mode in the oblate region of the flattening. This is consistent with the

projection induced modalities discussed earlier in Section 3.3. Nevertheless, the correct flattening value is clearly preferred. Because the projected track still encodes information about the underlying three-dimensional potential (see Appendix of [Nibauer et al. 2023](#)), the data retains discriminating power beyond simple sky projections. Our results show that even when working only with projected tracks, it is still possible to recover meaningful information about the full 3D potential. While being informative, the resulting posteriors are still relatively broad, which limits the strength of any single stream constraint on q . For this reason, in the next section we combine individual stream fits to obtain tighter constraints on the parameters of the underlying population distribution.

Before proceeding, it is important to acknowledge that our model isolates a single morphological parameter (q) within an idealised, axisymmetric potential. This simplification allows the population inference to focus exclusively on the halo flattening, neglecting all other inferred parameters. In reality, triaxiality, radially varying density profiles, and baryonic components (e.g. a disk) would introduce additional shape-related parameters and degeneracies, resulting in broader posteriors and a more complex population inference. These effects lie beyond the scope of the present work, which is intended to quantify the information content of the projected track in a controlled setting. Their impact will be explored in future studies.

4 POPULATION FIT

Beyond individual fits, our primary objective is to constrain the population distribution of halo flattening. While single stream fits may yield wide posteriors, we can combine them using hierarchical Bayesian inference to obtain robust constraints on population parameters and shed light on what is the morphology of DM halos considering the ensemble ([Chua et al. 2019](#); [Prada et al. 2019](#)).

We now consider a population of N streams. For stream n we denote its data by d_n and its parameters by θ_n . Let α be the hyperparameters that describe the population distribution of interest (here, the distribution of halo flattening q).

We assume that, conditioned on θ_n , the data sets $\{d_n\}$ are independent, and that the θ_n are drawn independently from a population prior $\pi(\theta_n|\alpha)$. The hyperprior on α is denoted by $\pi(\alpha)$.

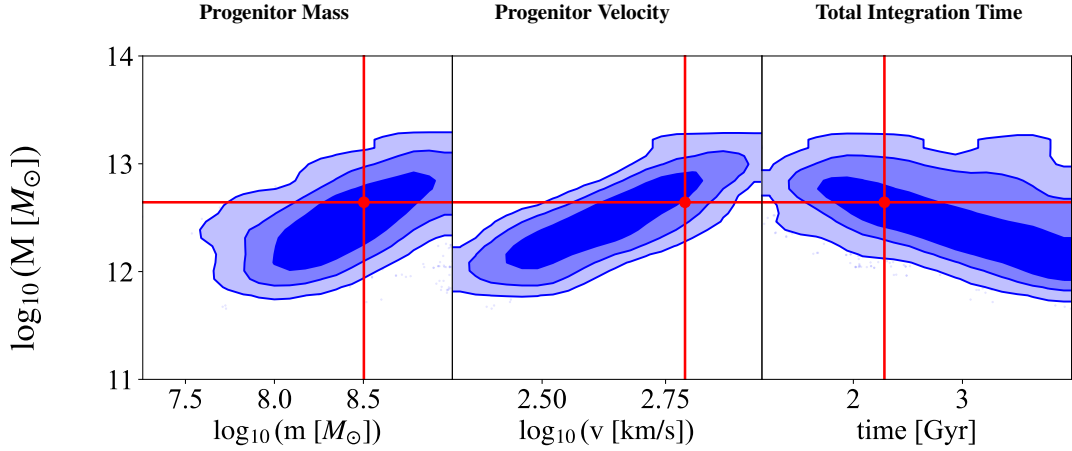


Figure 5. Joint posterior distributions showing the degeneracy of the mass of the halo ($\log_{10}(M [M_\odot])$) as a function of the mass of the progenitor ($\log_{10}(m [M_\odot])$), the velocity ($\log_{10}(v [\text{km/s}])$) and integration time. Ground truth is shown in red. Increasing the mass of the halo can be compensated by also increasing the mass and velocity of the progenitor while reducing the time. Without kinematic data these degeneracies cannot be broken.

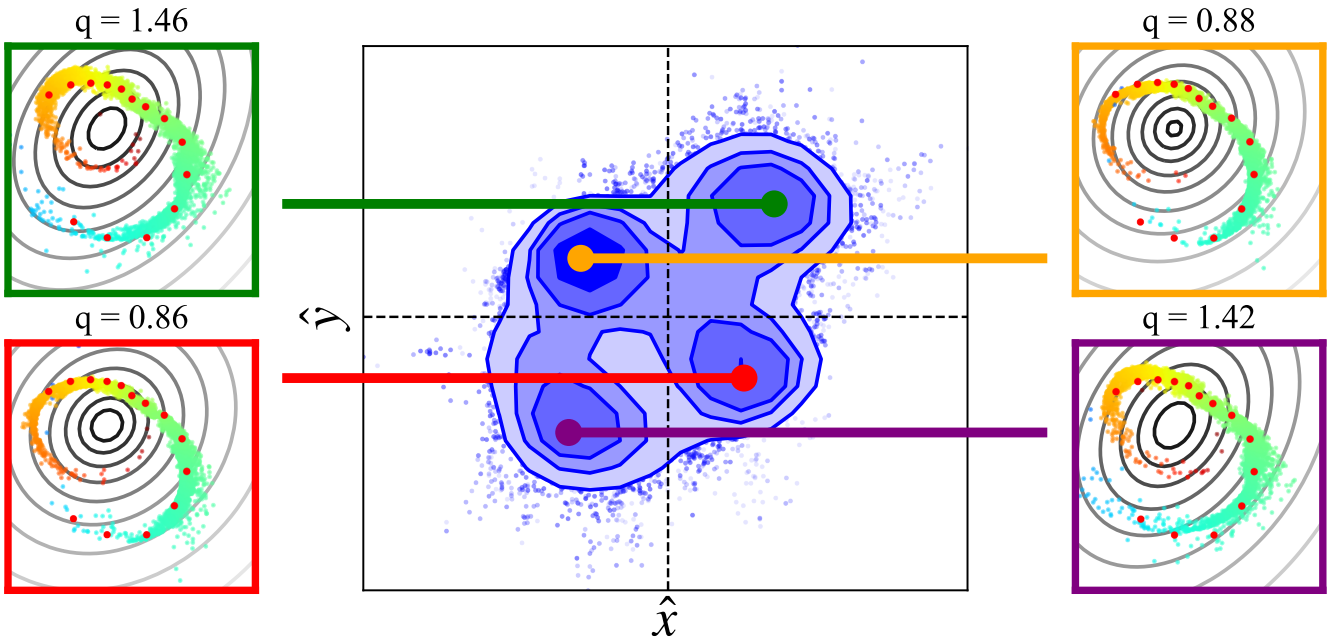


Figure 6. Zoom on the correlated posterior of the orientation from one mock stream track projected onto the XY -plane (the setting is the same than Figure 3). For each of the four visible modes we show the best-fit stream (rainbow ordering of the stream particles where bluer means further away from the progenitor clockwise and redder, anti-clockwise) atop the mock data (red) and the projected equipotentials as grey contours; the inferred flattening q is listed above each panel. Modes correspond to projected rotations and oblate versus prolate swaps that give similar projected potential.

The hierarchical posterior for α given all data $\{d_n\}_{n=1}^N$ is then

$$p(\alpha|\{d_n\}) \propto \pi(\alpha) \prod_{n=1}^N \int p(d_n|\theta_n) \pi(\theta_n|\alpha) d\theta_n, \quad (19)$$

where proportionality reflects omission of the global normalisation constant $p(\{d_n\})$. Evaluating this posterior directly would require refitting each individual model for every sample of α , yielding a computational cost of $O(N^2)$, which is infeasible given the cost of stream modeling and the large N required for tight constraints. Instead, we follow the reweighting approach introduced in Hogg et al.

(2010), which allows for a computationally efficient $O(N)$ solution. The key idea is to use the posterior samples from individual fits to recover the underlying likelihood.

Suppose we have already performed individual Bayesian inferences for each stream, using some prior $\pi(\theta_n)$ (not depending on α), and obtained the posterior

$$p(\theta_n|d_n) = \frac{p(d_n|\theta_n) \pi(\theta_n)}{Z_n}, \quad (20)$$

with

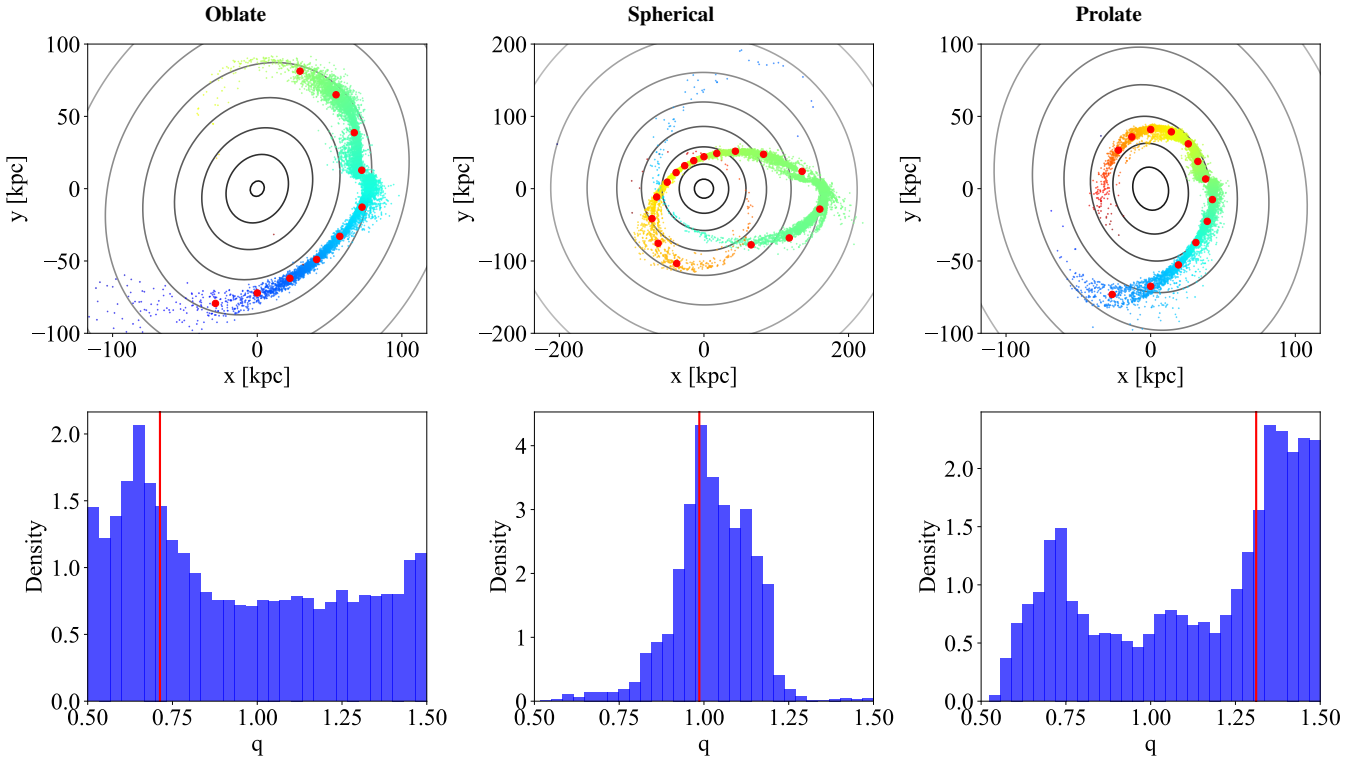


Figure 7. Examples of best-fit streams projected in the XY plane (top) and their posteriors for the flattening q (bottom). From left to right: oblate, spherical, and prolate cases, with the ground truth in red. In all three cases, the fits recover the mock tracks and the posterior on the flattening shows a preference for values close to the ground truth. The secondary mode in the prolate case (bottom right) reflects projection symmetries discussed in Section 3.3.

$$Z_n = p(d_n) = \int p(d_n|\theta_n) \pi(\theta_n) d\theta_n$$

the evidence for stream n under the individual prior.

Rearranging Eq. (20) gives

$$p(d_n|\theta_n) = \frac{p(\theta_n|d_n)}{\pi(\theta_n)} Z_n.$$

Substituting into Eq. (19),

$$p(\alpha|d_n) \propto \pi(\alpha) \prod_{n=1}^N \int \frac{p(\theta_n|d_n)}{\pi(\theta_n)} Z_n \pi(\theta_n|\alpha) d\theta_n \quad (23)$$

$$\propto \pi(\alpha) \prod_{n=1}^N \int p(\theta_n|d_n) \frac{\pi(\theta_n|\alpha)}{\pi(\theta_n)} d\theta_n, \quad (24)$$

where we have dropped the product of evidences $\prod_n Z_n$, which does not depend on α .

The integral in Eq. (24) is an expectation over the known posterior $p(\theta_n|d_n)$ and can be approximated with posterior samples. Let $\{\theta_{ni}\}_{i=1}^{K_n}$ be K_n samples from $p(\theta_n|d_n)$. Then

$$\int p(\theta_n|d_n) \frac{\pi(\theta_n|\alpha)}{\pi(\theta_n)} d\theta_n \approx \frac{1}{K_n} \sum_{i=1}^{K_n} p(\theta_{ni}|d_n) \frac{\pi(\theta_{ni}|\alpha)}{\pi(\theta_{ni})}. \quad (25)$$

Thus the hierarchical posterior can be approximated as

$$p(\alpha|d_n) \propto \pi(\alpha) \prod_{n=1}^N \left[\frac{1}{K_n} \sum_{i=1}^{K_n} p(\theta_{ni}|d_n) \frac{\pi(\theta_{ni}|\alpha)}{\pi(\theta_{ni})} \right]. \quad (26)$$

In the application of interest, the population model acts only on the halo flattening q . We decompose the parameters as

$$\theta_n = (q_n, \psi_n), \quad (27)$$

where ψ_n collects all nuisance parameters (e.g. halo mass, scale radius, progenitor phase-space coordinates). We assume that the individual prior factorises as

$$\pi(\theta_n) = \pi(q_n) \pi(\psi_n), \quad (28)$$

and that the population prior has the form

$$\pi(\theta_n|\alpha) = \pi(q_n|\alpha) \pi(\psi_n), \quad (29)$$

with the same prior $\pi(\psi_n)$ on the nuisance parameters. The ratio in Eq. (26) then simplifies to

$$\frac{\pi(\theta_{ni}|\alpha)}{\pi(\theta_{ni})} = \frac{\pi(q_{ni}|\alpha)}{\pi(q_{ni})}. \quad (30)$$

If the individual prior on q is uniform on $[q_{\min}, q_{\max}]$,

$$\pi(q_n) = \begin{cases} \frac{1}{q_{\max} - q_{\min}}, & q_{\min} \leq q_n \leq q_{\max}, \\ 0, & \text{otherwise,} \end{cases} \quad (31)$$

then $\pi(q_{ni})$ is a constant for all posterior samples used in the reweighting. That constant can be absorbed into the overall normalisation of $p(\alpha|{d_n})$, and we obtain

$$p(\alpha|{d_n}) \propto \pi(\alpha) \prod_{n=1}^N \left[\frac{1}{K_n} \sum_{i=1}^{K_n} p(q_{ni}|d_n) \pi(q_{ni}|\alpha) \right]. \quad (32)$$

Equation (32) is the working expression used to evaluate the hierarchical likelihood for any proposed hyperparameters α . This method is computationally efficient and scalable but relies on a critical condition: the conditional prior on the flattening, $\pi(q|\alpha)$, must lie within the actual prior, $\pi(q)$, used for the individual inference. Since no new samples are generated in this second-stage inference, the individual posteriors must already sufficiently cover the relevant parameter space. This is the case here since our individual posteriors on flattening are usually quite broad and very rarely completely rule out a region of parameter space.

As a concrete example, we consider a population model in which the physical flattening q is distributed as a Gaussian with mean μ_{pop} and standard deviation σ_{pop} , truncated to the same support as the individual prior, $[q_{\min}, q_{\max}]$. The hyperparameters are

$$\alpha = (\mu_{\text{pop}}, \sigma_{\text{pop}}). \quad (33)$$

The (unnormalised) Gaussian density is

$$\phi(q|\mu_{\text{pop}}, \sigma_{\text{pop}}) = \frac{1}{\sqrt{2\pi} \sigma_{\text{pop}}} \exp\left[-\frac{1}{2} \left(\frac{q - \mu_{\text{pop}}}{\sigma_{\text{pop}}}\right)^2\right]. \quad (34)$$

The truncated density is

$$\pi(q|\alpha) = \begin{cases} \frac{\phi(q|\mu_{\text{pop}}, \sigma_{\text{pop}})}{\Phi\left(\frac{q_{\max} - \mu_{\text{pop}}}{\sigma_{\text{pop}}}\right) - \Phi\left(\frac{q_{\min} - \mu_{\text{pop}}}{\sigma_{\text{pop}}}\right)}, & q_{\min} \leq q \leq q_{\max}, \\ 0, & \text{otherwise,} \end{cases} \quad (35)$$

where Φ is the standard normal cdf. In practice, when evaluating the reweighting factor $\pi(q_{ni}|\alpha)$ inside Eq. (32), it is sufficient to use the properly normalised truncated density (35). The hyperprior $\pi(\alpha)$ can be chosen, for example, as a product of broad uniform priors on μ_{pop} and σ_{pop} .

To initialize the different and separate population distributions, we generate N streams for each, drawing true values of q from one of three underlying population distributions assuming that all haloes are drawn from a single Gaussian population:

- (i) Oblate: $\mu_{\text{pop}} = 0.8$, $\sigma_{\text{pop}} = 0.1$,
- (ii) Spherical: $\mu_{\text{pop}} = 1.0$, $\sigma_{\text{pop}} = 0.1$,
- (iii) Prolate: $\mu_{\text{pop}} = 1.2$, $\sigma_{\text{pop}} = 0.1$.

For every data point in the dataset which represent a modelled stream, we first obtain the posterior on the flattening by performing N individual fits. In all the following examples, we set $N = 35$ motivated by STRRINGS (Sola et al. 2025). From there, we infer the population parameters $(\mu_{\text{pop}}, \sigma_{\text{pop}})$ through our Bayesian hierarchical inference pipeline using the same dynamic nested sampling implementation from *Dynesty*, this time with 500 live points. Given the low dimensionality, we use the uniform sampler, which helps accelerate the inference. The priors are uniform for both and range from $[0.5, 1.5]$ for μ_{pop} and $[0, 1]$ for σ_{pop} .

Figure 8 shows the posteriors of the average and standard deviation

of three different populations of modelled projected tracks. From left to right, the population distributions represent the situation (i), (ii) and (iii) as shown from the ground truth in red. Each population comprises 35 streams, chosen to mimic the STRRINGS catalogue. Even with our highly optimised population inference pipeline, obtaining posterior distributions for a single population requires roughly one week of computation. We therefore adopt a sample size large enough to constrain the parameters while keeping the computational cost manageable. Increasing the number of streams generally improves the precision and reduces bias in the inferred parameters, though this effect is not strictly linear. In practice, the total information content varies significantly between individual streams, so population level constraints depend on both the number and quality of the streams.

To explore this, we examined the absolute mean error as a function of stream length (both physical and angular), mean radial distance, and radial variation, finding no clear correlation (see Appendix A for more information). Although, since length typically increases the available phase-space information (Bonaca & Hogg 2018), individual streams are expected to yield better fits when longer, this effect does not translate straightforwardly to populations. As shown by Nibauer et al. (2023), the most constraining features in stream tracks for halo morphology are the straight segments. Because longer streams do not necessarily contain more of these segments, their contribution to the overall population level inference is not systematically stronger. Moreover, since we are constraining the halo flattening, an azimuthal property, the radial distance and variation of the track have little impact on the quality of the fits in contrast to Nibauer & Pearson (2025), who found a radial dependence when fitting for the host halo's radial density profile.

We see that in all three cases, the parameters are all confidently within 2σ . For the spherical case (middle panel), there is no bias in the posterior distribution of the mean position, μ , whereas for the oblate (left) and prolate (right) case there is a clear bias (larger tail) pointing towards the spherical case. We explain this from two phenomena. Firstly, we remark that the correct axis ratio is always the most extreme flattening. Indeed, any small deviations in orientation or measurement error tend to make the system appear more spherical. Secondly, the modalities between oblate and prolate discussed in Section 3.3 can also explain the bias towards the other end of the flattening space. Importantly, the multimodalities seen in some individual posteriors between oblate and prolate are completely absent at the population level. Just like μ , the posteriors on the standard deviations, σ , are confidently constrained but also exhibits bias towards larger deviation which also related to the two aforementioned reasons. A larger standard deviation for the population model helps better fit the outskirts of the distribution. Overall, we demonstrate that while individual projected stream tracks are weakly informative, fitting as few as 35 streams allows us to confidently constrain the population-level shape of dark matter haloes.

It is important to note that the fitted population model is assumed to match the true underlying distribution. In this work, we generate populations of axisymmetric haloes by sampling from a Gaussian distribution and subsequently fitting the parameters of that same Gaussian. In reality, the true distribution is unknown, and an incorrect model choice could lead to biased parameter estimates. However, cosmological simulations can provide physically motivated expectations for this population distribution and thus inform the choice of priors (Jing & Suto 2002b; Allgood et al. 2006; Bett et al. 2007; Vera-Ciro et al. 2011; Velliscig et al. 2015; Butsky et al. 2016; Chua et al. 2019). Moreover, this approach implicitly assumes that all haloes are drawn from a single population; relaxing this assumption to allow

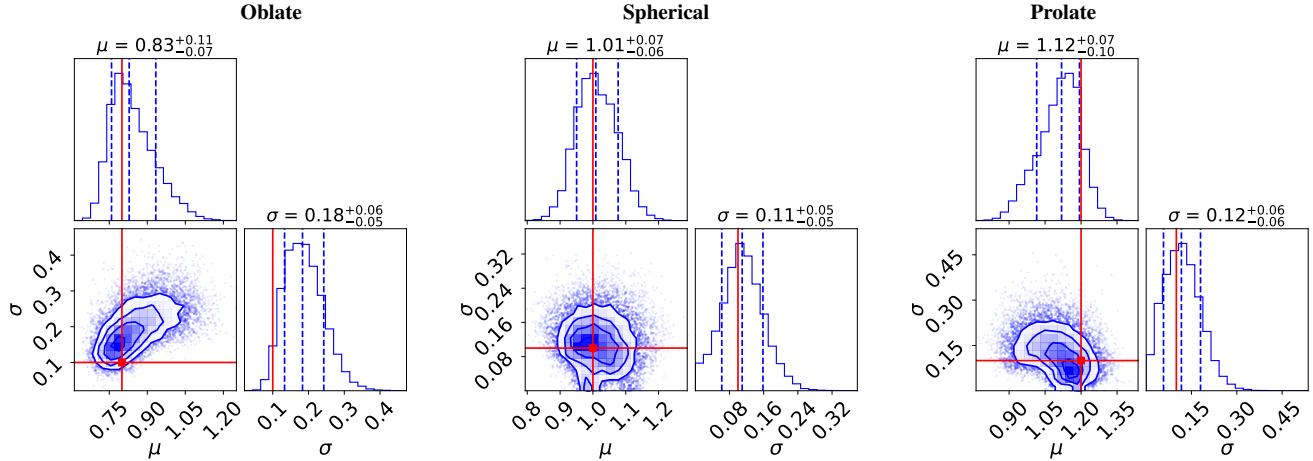


Figure 8. Posteriors on the parameters of the underlying population distribution of flattening for three distinct dark matter halo morphologies: oblate (left), spherical (middle) and prolate (right). Blue dashed vertical lines indicate the 16th, 50th, and 84th percentiles, corresponding to the median and $\pm 1\sigma$ intervals (values shown above each panel). These posteriors were obtained with three distinct populations of 35 streams each with the ground truth shown in red. We see a small bias towards more spherical halos for both the oblate and prolate distributions, this bias is not present in the spherical case. The standard deviation of the distribution also shows this bias. For all three cases, the ground truth is within 2σ of the inferred posterior distributions.

for mixtures of distinct halo populations will be the subject of future work.

5 DISCUSSION AND CONCLUSIONS

We developed a linearly scalable, JAX-accelerated hierarchical Bayesian framework to infer the population-level morphology of DM halos using tracks of projected stellar streams. Our stream generator, **StreaMAX** (Sola et al. 2025), achieves substantial speedups via compilation and vectorised parallelism. Tailored to extragalactic applications, our method extracts information from photometry alone, with no kinematic inputs. First, we fit streams individually leading to broad posterior on the halo flattening. Second, by treating the individual fits as a population, we combine individual posteriors and obtain tight constraints on the population level parameters.

Our main results are summarized as follows:

- (i) Forward modelling of stellar streams with a JAX-compiled particle-spray and dynamic nested sampling reliably recovers halo flattening q across oblate, spherical, and prolate morphologies, while limiting strong couplings with other (nuisance) parameters.
- (ii) Individual fits sometimes exhibit projection-induced multimodality between oblate and prolate solutions; at the population level these modes manifest as potential biases.
- (iii) Combining posteriors from 35 simulated streams accurately reconstructs the input shape distribution, demonstrating clear discrimination among oblate, spherical, and prolate populations.
- (iv) Population posteriors show a mild tendency toward rounder ($q \approx 1$) shapes and slightly inflated standard deviations, attributable to projection effects and sampling inefficiencies.

This study serves as a proof of concept for utilizing extragalactic streams for population inference of DM halos. Here, we address some of the limitations of this work given our assumptions:

- (i) We fit only the ridgeline (track) in projection, discarding width and surface density information. Using these observables will require a more realistic stream model (e.g. mass loss and variable spray emission) and a likelihood that models not only position but also width and density.

(ii) One projected progenitor coordinate is fixed, effectively assuming a known on-track position. A more general parameterisation would allow the progenitor to slide freely along the track.

(iii) The host potential is intentionally simplified (axisymmetric NFW, no baryons) making flattening the only parameter dictating the shape of the halo. This allowed us to constrain population parameters without having to worry about degeneracies amongst morphological parameters. Allowing triaxiality, radial profile variations, and baryonic components will introduce additional, physically relevant degeneracies.

(iv) All tests are closed loop: mocks and fits share the same forward model and noise, and the population prior and likelihood families match. This allowed testing the capabilities of our pipeline without worrying about biases, but we stress that real data will inevitably violate these assumptions, and model mismatch can bias inferences.

Our computationally efficient framework is well suited to upcoming wide-field imaging from Euclid and Rubin/LSST, which will vastly expand the census of extragalactic streams, creating unprecedented opportunities for population-level analyses. Looking ahead, we plan to refine our approach by incorporating additional stream properties, such as widths of the stream along the track, and allow for the progenitor to move completely freely in the projected plane. Furthermore, we are working on more accurately modeling the host's potential by also fitting for the baryonic matter of the galaxy. We are also exploring more complex dark matter halo distributions and the effect of assuming the wrong underlying population distribution on our retrieval.

In a future work, we will apply this methodology to observations using the STRINGS catalogue (Sola et al. 2025) of 35 faint, curved, and extended streams identified in the Dark Energy Spectroscopic Instrument Legacy Imaging Surveys (DESI-LS; Dey et al. 2019). To our knowledge, this will provide the first population scale constraints on dark matter halo shapes derived from stellar streams in external galaxies.

ACKNOWLEDGEMENTS

The authors would like to thank Tom Hehir, Chris Moore and Kaisey Mandel for their valuable insight. DC acknowledges funding from the Harding Distinguished Postgraduate Scholars Program. ES is grateful to the Leverhulme Trust for funding under the grant number RPG-2021-205.

DATA AVAILABILITY

All data used in this work were generated through simulations using code developed by the authors. The model used to simulate stream tracks is publicly available as a Python package on [StreaMAX](#). The full fitting pipeline, along with scripts to reproduce all figures and results, is available upon request.

REFERENCES

Abbott T. M. C., et al., 2018, *ApJS*, **239**, 18

Allgood B., Flores R. A., Primack J. R., Kravtsov A. V., Wechsler R. H., Faltenbacher A., Bullock J. S., 2006, *MNRAS*, **367**, 1781

Amorisco N. C., 2015, *MNRAS*, **450**, 575

Amorisco N. C., Martinez-Delgado D., Schedler J., 2015, *arXiv e-prints*, p. [arXiv:1504.03697](#)

Atkinson A. M., Abraham R. G., Ferguson A. M. N., 2013, *ApJ*, **765**, 28

Bailin J., Steinmetz M., 2005, *ApJ*, **627**, 647

Banik N., Bovy J., 2019, *MNRAS*, **484**, 2009

Banik N., Bovy J., Bertone G., Erkal D., de Boer T. J. L., 2021, *J. Cosmology Astropart. Phys.*, **2021**, 043

Bayes M., Price M., 1763, *Philosophical Transactions of the Royal Society of London Series I*, **53**, 370

Belokurov V., et al., 2014, *MNRAS*, **437**, 116

Bett P., Eke V., Frenk C. S., Jenkins A., Helly J., Navarro J., 2007, *Monthly Notices of the Royal Astronomical Society*, **376**, 215

Bett P., Eke V., Frenk C. S., Jenkins A., Okamoto T., 2010, *MNRAS*, **404**, 1137

Bílek M., et al., 2020, *MNRAS*, **498**, 2138

Binney J., 2008, *MNRAS*, **386**, L47

Blumenthal G. R., Faber S. M., Flores R., Primack J. R., 1986, *ApJ*, **301**, 27

Bonaca A., Hogg D. W., 2018, *ApJ*, **867**, 101

Bonaca A., Price-Whelan A. M., 2025, *New Astron. Rev.*, **100**, 101713

Bonaca A., Geha M., Küpper A. H. W., Diemand J., Johnston K. V., Hogg D. W., 2014, *ApJ*, **795**, 94

Bonaca A., Hogg D. W., Price-Whelan A. M., Conroy C., 2019, *ApJ*, **880**, 38

Bonamigo M., Despali G., Limousin M., Angulo R., Giocoli C., Soucail G., 2015, *MNRAS*, **449**, 3171

Bovy J., 2014, *ApJ*, **795**, 95

Bovy J., Bahmanyar A., Fritz T. K., Kallivayalil N., 2016, *ApJ*, **833**, 31

Bowden A., Belokurov V., Evans N. W., 2015, *MNRAS*, **449**, 1391

Boylan-Kolchin M., Ma C.-P., Quataert E., 2006, *MNRAS*, **369**, 1081

Bradbury J., et al., 2018, JAX: composable transformations of Python+NumPy programs, <http://github.com/jax-ml/jax>

Bryan S. E., Kay S. T., Duffy A. R., Schaye J., Dalla Vecchia C., Booth C. M., 2013, *MNRAS*, **429**, 3316

Bullock J. S., Johnston K. V., 2005, *ApJ*, **635**, 931

Butsky I. S., et al., 2016, *Monthly Notices of the Royal Astronomical Society*, **462**, 663

Carlberg R. G., Grillmair C. J., Hetherington N., 2012, *ApJ*, **760**, 75

Carlin J. L., Beaton R. L., Martinez-Delgado D., Gabany R. J., 2016, in Newberg H. J., Carlin J. L., eds, *Astrophysics and Space Science Library* Vol. 420, *Tidal Streams in the Local Group and Beyond*. p. 219 ([arXiv:1603.04656](#)), doi:10.1007/978-3-319-19336-6_9

Chen Y., Valluri M., Gnedin O. Y., Ash N., 2025, *ApJS*, **276**, 32

Choi J.-H., Weinberg M. D., Katz N., 2007, *Monthly Notices of the Royal Astronomical Society*, **381**, 987–1000

Chua K. T. E., Pillepich A., Vogelsberger M., Hernquist L., 2019, *MNRAS*, **484**, 476

Codis S., Pichon C., Pogosyan D., 2015, *MNRAS*, **452**, 3369

Crnojević D., et al., 2016, *ApJ*, **823**, 19

Cui X.-Q., et al., 2012, *Research in Astronomy and Astrophysics*, **12**, 1197

Deason A. J., Belokurov V., 2024, *New Astron. Rev.*, **99**, 101706

Debattista V. P., Roškar R., Valluri M., Quinn T., Moore B., Wadsley J., 2013, *MNRAS*, **434**, 2971

Despali G., Giocoli C., Tormen G., 2014, *MNRAS*, **443**, 3208

Dey A., et al., 2019, *AJ*, **157**, 168

Di Cintio A., Brook C. B., Macciò A. V., Stinson G. S., Knebe A., Dutton A. A., Wadsley J., 2014, *MNRAS*, **437**, 415

Diemer B., Kravtsov A. V., 2015, *ApJ*, **799**, 108

Dillamore A. M., Belokurov V., Evans N. W., Price-Whelan A. M., 2022, *MNRAS*, **516**, 1685

Dutton A. A., Macciò A. V., 2014, *MNRAS*, **441**, 3359

Erkal D., Belokurov V., 2015, *MNRAS*, **450**, 1136

Erkal D., Belokurov V., Bovy J., Sanders J. L., 2016, *MNRAS*, **463**, 102

Erkal D., Koposov S. E., Belokurov V., 2017, *MNRAS*, **470**, 60

Erkal D., et al., 2019, *MNRAS*, **487**, 2685

Errani R., Peñarrubia J., 2020, *MNRAS*, **491**, 4591

Eyre A., Binney J., 2011, *MNRAS*, **413**, 1852

Fakhouri O., Ma C.-P., Boylan-Kolchin M., 2010, *MNRAS*, **406**, 2267

Fardal M. A., et al., 2013, *MNRAS*, **434**, 2779

Fardal M. A., Huang S., Weinberg M. D., 2015, *MNRAS*, **452**, 301

Gaia Collaboration et al., 2018, *A&A*, **616**, A1

Gaia Collaboration et al., 2021, *A&A*, **649**, A1

Gibbons S. L. J., Belokurov V., Evans N. W., 2014, *MNRAS*, **445**, 3788

Gnedin O. Y., Kravtsov A. V., Klypin A. A., Nagai D., 2004, *ApJ*, **616**, 16

Grillmair C. J., Dionatos O., 2006, *ApJ*, **643**, L17

Harris W. E., 1996, *AJ*, **112**, 1487

Harris W. E., 2010, *arXiv e-prints*, p. [arXiv:1012.3224](#)

Hayashi E., Navarro J. F., Taylor J. E., Stadel J., Quinn T., 2003, *ApJ*, **584**, 541

Helmi A., White S. D. M., 1999, *MNRAS*, **307**, 495

Hendel D., Johnston K. V., 2015, *MNRAS*, **454**, 2472

Higson E., Handley W., Hobson M., Lasenby A., 2019, *Statistics and Computing*, **29**, 891

Hockney R. W., Eastwood J. W., 1988, *Computer simulation using particles*

Hogg D. W., Myers A. D., Bovy J., 2010, *ApJ*, **725**, 2166

Hood C. E., Kannappan S. J., Stark D. V., Dell'Antonio I. P., Moffett A. J., Eckert K. D., Norris M. A., Hendel D., 2018, *ApJ*, **857**, 144

Ibata R., Lewis G. F., Irwin M., Totten E., Quinn T., 2001, *ApJ*, **551**, 294

Ibata R. A., Lewis G. F., Irwin M. J., Quinn T., 2002, *MNRAS*, **332**, 915

Ivezić Ž., et al., 2019, *ApJ*, **873**, 111

Jing Y. P., Suto Y., 2002a, *ApJ*, **574**, 538

Jing Y. P., Suto Y., 2002b, *The Astrophysical Journal*, **574**, 538

Johnston K. V., 1998, *ApJ*, **495**, 297

Johnston K. V., Spergel D. N., Hernquist L., 1995, *ApJ*, **451**, 598

Johnston K. V., Sackett P. D., Bullock J. S., 2001, *ApJ*, **557**, 137

Johnston K. V., Spergel D. N., Haydn C., 2002, *ApJ*, **570**, 656

Johnston K. V., Law D. R., Majewski S. R., 2005, *ApJ*, **619**, 800

King I., 1962, *AJ*, **67**, 471

Koposov S. E., Rix H.-W., Hogg D. W., 2010, *ApJ*, **712**, 260

Koposov S. E., et al., 2019, *MNRAS*, **485**, 4726

Koposov S., et al., 2022, *joshspeagle/dynesty*: v2.0.3, doi:10.5281/zenodo.7388523

Koposov S. E., et al., 2023, *MNRAS*, **521**, 4936

Küpper A. H. W., Lane R. R., Heggie D. C., 2012, *MNRAS*, **420**, 2700

Küpper A. H. W., Balbinot E., Bonaca A., Johnston K. V., Hogg D. W., Kroupa P., Santiago B. X., 2015, *ApJ*, **803**, 80

LSST Science Collaboration et al., 2009, *arXiv e-prints*, p. [arXiv:0912.0201](#)

Laine S., et al., 2018, *arXiv e-prints*, p. [arXiv:1812.04897](#)

Laureijs R., et al., 2011, *arXiv e-prints*, p. [arXiv:1110.3193](#)

Law D. R., Majewski S. R., 2010, *ApJ*, **714**, 229

Li T. S., et al., 2019, *MNRAS*, **490**, 3508

Li T. S., et al., 2022, *ApJ*, **928**, 30

Lovell M. R., Frenk C. S., Eke V. R., Jenkins A., Gao L., Theuns T., 2014, *MNRAS*, **439**, 300

Ludlow A. D., Navarro J. F., Angulo R. E., Boylan-Kolchin M., Springel V., Frenk C., White S. D. M., 2014, *MNRAS*, **441**, 378

Macciò A. V., Dutton A. A., van den Bosch F. C., 2008, *MNRAS*, **391**, 1940

Majewski S. R., et al., 2017, *AJ*, **154**, 94

Malhan K., Ibata R. A., 2019, *MNRAS*, **486**, 2995

Malhan K., Ibata R. A., Martin N. F., 2018, *MNRAS*, **481**, 3442

Mancillas B., Duc P.-A., Combes F., Bournaud F., Emsellem E., Martig M., Michel-Dansac L., 2019, *A&A*, **632**, A122

Martínez-Delgado D., et al., 2010, *AJ*, **140**, 962

Martínez-Delgado D., et al., 2023, *A&A*, **671**, A141

McConnachie A. W., 2012, *AJ*, **144**, 4

Miró-Carretero J., et al., 2024, *A&A*, **691**, A196

Mouhcine M., Ibata R., Rejkuba M., 2010, *ApJ*, **714**, L12

Navarro J. F., Frenk C. S., White S. D. M., 1997, *ApJ*, **490**, 493

Nibauer J., Bonaca A., 2025, *ApJ*, **985**, L22

Nibauer J., Pearson S., 2025, *arXiv e-prints*, p. arXiv:2508.02666

Nibauer J., Bonaca A., Johnston K. V., 2023, *ApJ*, **954**, 195

Nibauer J., Bonaca A., Price-Whelan A. M., Spergel D. N., Greene J. E., 2025, *arXiv e-prints*, p. arXiv:2510.02247

Palau C. G., Miralda-Escudé J., 2023, *MNRAS*, **524**, 2124

Peñarrubia J., McConnachie A. W., Navarro J. F., 2008, *ApJ*, **672**, 904

Pearson S., Küpper A. H. W., Johnston K. V., Price-Whelan A. M., 2015, *ApJ*, **799**, 28

Pearson S., Starkenburg T. K., Johnston K. V., Williams B. F., Ibata R. A., Khan R., 2019, *ApJ*, **883**, 87

Pearson S., Price-Whelan A. M., Hogg D. W., Seth A. C., Sand D. J., Hunt J. A. S., Crnojević D., 2022, *ApJ*, **941**, 19

Pearson S., Bonaca A., Chen Y., Gnedin O. Y., 2024, *ApJ*, **976**, 54

Peter A. H. G., Rocha M., Bullock J. S., Kaplinghat M., 2013, *MNRAS*, **430**, 105

Prada J., Forero-Romero J. E., Grand R. J. J., Pakmor R., Springel V., 2019, *MNRAS*, **490**, 4877

Price-Whelan A. M., 2017, *The Journal of Open Source Software*, 2

Price-Whelan A. M., Bonaca A., 2018, *ApJ*, **863**, L20

Price-Whelan A. M., Hogg D. W., Johnston K. V., Hendel D., 2014, *ApJ*, **794**, 4

Rocha M., Peter A. H. G., Bullock J. S., Kaplinghat M., Garrison-Kimmel S., Oñorbe J., Moustakas L. A., 2013, *MNRAS*, **430**, 81

Sameie O., Creasey P., Yu H.-B., Sales L. V., Vogelsberger M., Zavala J., 2018, *MNRAS*, **479**, 359

Sanders J. L., 2014, *MNRAS*, **443**, 423

Sanders J. L., Binney J., 2013, *MNRAS*, **433**, 1813

Sanders J. L., Bovy J., Erkal D., 2016, *MNRAS*, **457**, 3817

Shao S., Cautun M., Frenk C. S., Gao L., Crain R. A., Schaller M., Schaye J., Theuns T., 2016, *MNRAS*, **460**, 3772

Shipp N., et al., 2018, *ApJ*, **862**, 114

Sola E., et al., 2022, *A&A*, **662**, A124

Sola E., et al., 2025, *arXiv e-prints*, p. arXiv:2508.02154

Speagle J. S., 2020, *MNRAS*, **493**, 3132

Tal T., van Dokkum P. G., Nelan J., Bezanson R., 2009, *AJ*, **138**, 1417

Tempel E., Libeskind N. I., 2013, *ApJ*, **775**, L42

Tenneti A., Mandelbaum R., Di Matteo T., 2016, *MNRAS*, **462**, 2668

Tulin S., Yu H.-B., 2018, *Phys. Rep.*, **730**, 1

Valluri M., et al., 2025, *ApJ*, **980**, 71

Varghese A., Ibata R., Lewis G. F., 2011, *MNRAS*, **417**, 198

Vasiliev E., 2019, *MNRAS*, **482**, 1525

Vasiliev E., Belokurov V., Erkal D., 2021, *MNRAS*, **501**, 2279

Velliscig M., et al., 2015, *Monthly Notices of the Royal Astronomical Society*, **453**, 721

Vera-Ciro C., Helmi A., 2013, *ApJ*, **773**, L4

Vera-Ciro C. A., Helmi A., Starkenburg E., Breddels M. A., 2011, *Monthly Notices of the Royal Astronomical Society*, **416**, 1377

Walder M., Erkal D., Collins M., Martinez-Delgado D., 2024, *arXiv e-prints*, p. arXiv:2402.13314

Wechsler R. H., Bullock J. S., Primack J. R., Kravtsov A. V., Dekel A., 2002, *ApJ*, **568**, 52

Weerasooriya S., Starkenburg T., Cunningham E. C., Johnston K. V., 2025, *arXiv e-prints*, p. arXiv:2505.14792

Welker C., et al., 2020, *MNRAS*, **491**, 2864

Yavetz T. D., Johnston K. V., Pearson S., Price-Whelan A. M., Hamilton C., 2023, *ApJ*, **954**, 215

Yoon J. H., Johnston K. V., Hogg D. W., 2011, *ApJ*, **731**, 58

Yoon Y., Ko J., Chung H., Byun W., Chun K., 2024, *ApJ*, **965**, 158

York D. G., et al., 2000, *AJ*, **120**, 1579

Zhao D. H., Mo H. J., Jing Y. P., Börner G., 2003, *MNRAS*, **339**, 12

de Boer T. J. L., Belokurov V., Koposov S. E., Ferrarese L., Erkal D., Côté P., Navarro J. F., 2018, *MNRAS*, **477**, 1893

de Boer T. J. L., Erkal D., Gieles M., 2020, *MNRAS*, **494**, 5315

van Dokkum P., et al., 2019, *ApJ*, **883**, L32

APPENDIX A: POPULATION RELATIONS

Here we examine how the accuracy of the inferred flattening varies with simple morphological properties of the stream tracks across our full population. In total, we analyse the 105 individual posteriors obtained from this work. For each posterior we compute the absolute mean error (AME), which measures the average deviation of the posterior samples from the true value. Smaller AME values correspond to more accurate constraints.

For each stream we compute four descriptive quantities: angular length, physical length, mean distance from the origin, and radial distance spread (Figure A1). Angular lengths are discrete because tracks are binned in angle; the remaining quantities are continuous. Across the population, the scatter in AME at fixed morphological properties is large, and no single parameter produces a clean predictive trend. Nonetheless, we use linear regression to describe the correlation between the AME and our aformentioned quantities. Longer angular tracks exhibit slightly smaller errors, consistent with the idea that a greater number of angular bins provides more information. A similar trend appears with physical length: longer streams tend to have marginally lower AME, though this can be partly a geometric effect since the same angular extent corresponds to larger physical lengths at larger distances. The mean distance shows the opposite behaviour. Streams at smaller mean distance are more likely to cover larger angular extents, and thus modestly lower AME values. Finally, the radial distance spread shows almost no relation with AME. This is expected, as the flattening parameter primarily affects the angular structure of the orbit; probing a wider radial range is not required to constrain q in the projected track setting explored here.

Overall, while some qualitative trends exist, the intrinsic scatter is substantial. A larger and more diverse population of mock streams would be needed to assess the robustness of these relations and to quantify the sources of spread.

This paper has been typeset from a *TeX/LaTeX* file prepared by the author.

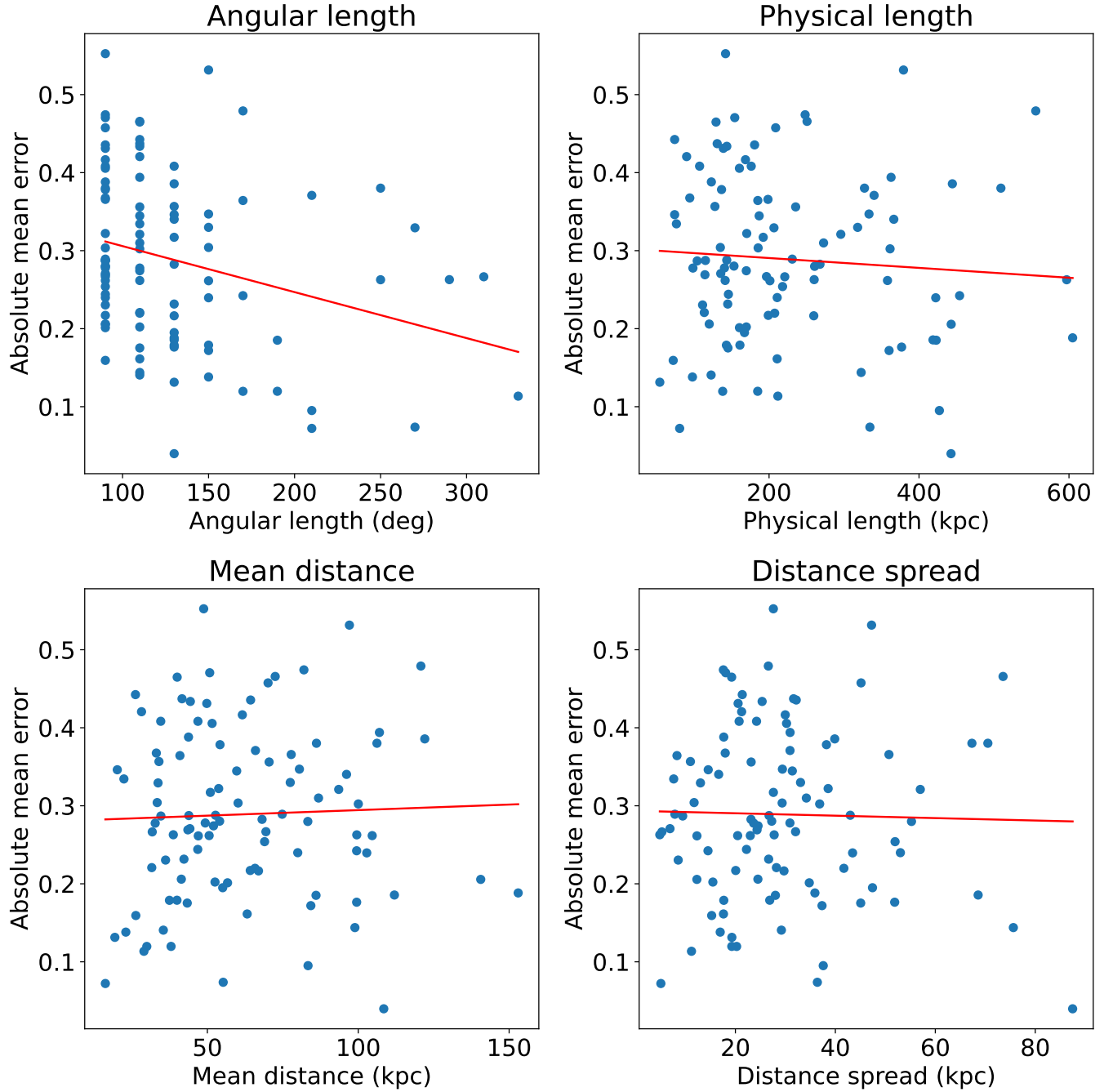


Figure A1. Absolute mean error of the inferred flattening for 105 stream fits as a function of four morphological properties of each stream: angular length, linear length, mean distance, and radial distance spread. The red line shows a simple linear fit. Weak trends are present but the overall scatter is large, and no single morphological parameter reliably predicts inference quality. That being said, longer streams (both angular and linear) tend to yield smaller errors, shorter mean distances also lead to smaller errors, and radial distance spread has no effect.